Available online at www.sciencedirect.com

ScienceDirect

Journal of Computational Physics 227 (2008) 9021–9043

JOURNAL OF COMPUTATIONAL PHYSICS

www.elsevier.com/locate/jcp

Impact of a vortex ring on a density interface using a regularized inviscid vortex sheet method

Mark J. Stock [a,*], Werner J.A. Dahm [b], Grétar Tryggvason [c]

[a] *Applied Scientific Research Inc., Santa Ana, CA 92705-5803, USA*
[b] *Laboratory for Turbulence and Combustion (LTC), Department of Aerospace Engineering, University of Michigan, Ann Arbor, MI 48109-2140, USA*
[c] *Department of Mechanical Engineering, Worcester Polytechnic Institute, Worcester, MA 01609-2280, USA*

Received 29 April 2007; received in revised form 19 April 2008; accepted 23 May 2008
Available online 7 June 2008

Abstract

A new, fully three-dimensional, vortex-in-cell method designed to follow the unsteady motion of inviscid vortex sheets with or without small (Boussinesq) density discontinuities is presented. As is common in front-tracking methods, the vortex sheet is described by a moving, unstructured mesh consisting of points connected by triangular elements. Each element carries scalar-valued circulations on its three edges, which can be used to represent any tangent vector value and in the present method represent the element's vorticity. As the interface deforms, nodes and elements are added and removed to maintain the resolution of the sheet and of the vortex sheet strength. The discretization and remeshing methods allow automatic, near-perfect conservation of circulation despite repeated stretching and folding of the interface. Results are compared with previous experiments and simulations. Similarities are observed between the present simulations and experiments of a vortex ring impacting a wall.

Keywords: Vortex methods; Vortex sheet dynamics; Vortex-in-cell; Stratified flow; Density discontinuity

---

1. Introduction

Vortex sheets are important in many areas of physics: they are generated on density discontinuities in multiphase flows through the action of gravity or shocks, are created by large-scale flow separation from bluff bodies, and are a source of instability in transitional and turbulent flows. Numerically predicting their complex, unsteady dynamics, however, has been a continuing challenge.

Lagrangian vortex methods have received much attention in recent years as an alternative to traditional grid-based Navier–Stokes and Euler solvers because of their immunity to numerical convective instability and the availability of fast solvers. They also gain advantage if the volume of fluid with significant vorticity magnitude is a small fraction of the total flow volume, as is the case with high Reynolds number flows. In these

---

[*] Corresponding author. Tel.: +1 734 644 8950.
E-mail address: mstock@umich.edu (M.J. Stock).

doi:10.1016/j.jcp.2008.05.022

cases, the flow can be represented in a more compact form by vorticity than is possible with velocity. This fact lends support to computational methods in vorticity variables.

The linear stability analysis of the vortex sheet equations shows that short-wavelength solutions have arbitrarily large growth rates (the Kelvin–Helmholtz instability), making the initial value problem ill-posed. Early studies of vortex sheet motion using point-vortex particles resulted in seemingly random behavior after a finite time [1] which was later shown to be singularity formation [2,3]. Desingularizing the vorticity allowed simulations to progress past the time of singularity formation, making long-time analysis of vortex sheet motion possible [4,5]. Regularized solutions have since been shown to approximate Navier–Stokes solutions for small enough viscosity and regularization length [6,7]. Regularization in vortex methods is usually introduced into Lagrangian methods by finite-sized vortex cores [4,5] and in Eulerian or hybrid Lagrangian–Eulerian methods by grid interpolation and/or cancellation [8,9].

First to speed up the direct $\mathcal{O}(N^2)$ calculation of Lagrangian vortex dynamics was Christiansen [8], who extended the cloud-in-cell technique [10] to vortex particles by solving a Poisson equation for streamfunction on a temporary Eulerian grid. This vortex-in-cell (VIC) algorithm reduces the cost per time step to $\mathcal{O}(N + M\log_2 M)$, where N is the number of vortex elements and M is the number of cells in the grid. Couët [11] demonstrated the first three-dimensional VIC method, which solved for the motion of vortex filaments to study the evolution of vortex rings. Because the solution is computed on a grid, the finest scales of motion are limited to the size of a cell.

The Lagrangian elements that represent the vorticity can take the form of particles, filaments, sheets, or discrete volumes. The choice of discretization technique dictates the methods that must be used for operations such as diffusion, remeshing to maintain accuracy, and accounting for vortex stretching.

The most popular discretization for two- and three-dimensional vortex methods has been particles. Particles require no neighbor connectivity information, simplifying programming effort. They can be remeshed using a regular grid with only minor losses [12]. They support diffusion methods easily [13,14]. They suffer from some drawbacks: the vortex stretching term must be accounted for by calculating the velocity gradient at each particle location for each timestep [15], and frequent regridding must be done to prevent particle separation and the accompanying loss of accuracy. They cannot easily track surfaces of discontinuity.

Early research [16–18] recognized the algorithmic benefits of using connected segments in three dimensions to represent vortex filaments. As the Lagrangian nodes move and separate, the segments connecting them rotate and elongate. Kelvin's circulation theorem states that the circulations on these segments do not change. So, in filament methods the vorticity is automatically divergence-free, and circulation is conserved because the filaments are transported with unchanged circulation. Filaments are easy to remesh along their length, and "filament surgery" can account for localized cancellation of oppositely-signed vorticity [16,19,20]. Unfortunately, it becomes inefficient or computationally expensive to remesh in cross-filament directions, as would be required to maintain resolution after diffusion, or when stretch acts perpendicular to the filaments [21], or when a collection of separate filaments is used to represent a continuous vortex sheet [22–24].

Efficiently tracking vortex sheets in three dimensions, however, requires not only element connectivity in two local dimensions, but a method to prevent excessive detail below the regularization length scale. Several vortex sheet methods have been proposed, but few address all of these concerns.

A vortex sheet method can exist without remeshing [6,25], but would suffer from either limited applicability to problems with low in-sheet strain or from lack of intermediate- to long-time simulation accuracy. Other research introduced new methods for integrating the singular Biot–Savart kernel over a surface [26–28], but the resulting dynamic vortex methods also do not provide for remeshing.

Brady et al. [29] maps the entire vortex sheet onto a parametric plane and performs global remeshing which results in higher resolution in areas with high mean curvature. This does not allow long-time runs because material sheets in unsteady flows quickly create areas of high curvature that could remain unresolved in regularized methods. The Eulerian level-set method of Harabetian et al. [9] performs global "remeshing" by locating the vortex sheet with a scalar marker function that forces potentially-unphysical topology changes when surfaces close to within one grid cell.

Lindsay and Krasny [21] remeshed vortex sheets by inserting either points along filaments or whole new filaments, depending on the direction of strain. The requirement to insert a whole filament when only a portion of its length may need the increased resolution is a source of inefficiency in this semi-local remeshing method.

Fully-local remeshing is done by Knio and Ghoniem [30–32], whose method tracks a scalar layer with triangular and quadrilateral elements while discretizing the vorticity as filaments. The local remeshing, though, is performed only along the edges of the quadrilaterals. As such, the method will always create great numbers of very thin elements because it can only efficiently adapt to strain perpendicular to the quadrilateral elements' edges. This is similar to the method of Kaganovskiy [33].

The proposed method remeshes locally and avoids all of the above difficulties by using a triangular mesh front-tracking method similar to [34] with a vorticity discretization scheme that can use either edge circulations or bound vortex sheet strength where algorithmically advantageous.

Contributions of the present work include: (1) a new Lagrangian vortex sheet method for long-running simulations of complex flows, (2) introduction of a vortex *sheet* discretization method that conserves circulation by design, (3) demonstration of a method for *localized* remeshing of vortex sheet geometry that is extensible to non-manifold recoalescence, and (4) new results for three-dimensional vortex rings impacting a density interface using an Euler method with regularization that compare favorably with previous physical and numerical experiments.

This paper is structured as follows. In the section below, the basic equations of vortex sheet motion and strength evolution are presented. Section 3 introduces the numerical method that solves these equations. Section 4 shows the results obtained by applying the method to several fully three-dimensional flow problems and discusses the conservation properties and other important aspects of the method. A summary of the results appears in Section 5.

2. Governing equations for vortex sheet dynamics

The vectorial strength γ of a three-dimensional vortex sheet separating inviscid fluids can be written as

$$\gamma = \hat{\boldsymbol{n}} \times (\boldsymbol{u}_1 - \boldsymbol{u}_2) = \hat{\boldsymbol{n}} \times \Delta\boldsymbol{u}, \tag{1}$$

where $\boldsymbol{u}_i$ is the value of velocity on either side of the vortex sheet, and $\hat{\boldsymbol{n}}$ is the sheet's local unit normal vector. The vortex sheet strength is related to the vorticity by

$$\boldsymbol{\omega} = \gamma\ \delta(n), \tag{2}$$

where δ is Dirac's delta function, and n is the distance normal to the sheet.

If this sheet is situated on an interface between immiscible fluids of possibly different densities, and the material marker velocities are equal to the average of the velocity on both sides of the sheet, then the evolution equation for the incompressible, inviscid sheet strength with zero surface tension [25,27,35] is

$$\frac{\mathrm{D}\gamma}{\mathrm{D}t} = \gamma \cdot \nabla\boldsymbol{u} + 2\ A\ \hat{\boldsymbol{n}} \times (\bar{\boldsymbol{a}} - \boldsymbol{g}), \tag{3}$$

$$\bar{\boldsymbol{a}} = \frac{\mathrm{D}\boldsymbol{u}}{\mathrm{D}t} + \frac{1}{4}\ \Delta\boldsymbol{u} + \nabla\Delta\boldsymbol{u}, \tag{4}$$

$$\frac{\mathrm{D}}{\mathrm{D}t} \equiv \frac{\partial}{\partial t} + \boldsymbol{u} \cdot \nabla, \tag{5}$$

where $\bar{\boldsymbol{a}}$ is the average of the fluid acceleration on both sides of the vortex sheet, $\boldsymbol{g}$ is the gravity vector, and A, the Atwood number, is equal to

$$A = \frac{\rho_2 - \rho_1}{\rho_2 + \rho_1}. \tag{6}$$

This equation can be non-dimensionalized using the following quantities:

$$\begin{aligned} \tilde{t} &= t\left(\frac{A||\boldsymbol{g}||}{R}\right)^{\frac{1}{2}} \quad \tilde{\gamma} = \gamma(A||\boldsymbol{g}||R)^{-\frac{1}{2}}, \\ \tilde{\boldsymbol{u}} &= \boldsymbol{u}(A||\boldsymbol{g}||R)^{-\frac{1}{2}} \quad \widetilde{\nabla} = \nabla R, \end{aligned} \tag{7}$$

where R is a representative length scale.

In the present method, it shall be assumed that the density jump is small ($\Delta\rho/\rho \ll 1$, thus $A \to 0$) and that the Froude number is large (or $||\boldsymbol{g}|| \to \infty$), such that the coefficient of the baroclinic term is constant and finite: $A||\boldsymbol{g}|| \equiv \theta = 1$. Under these assumptions, the coefficient on the term representing baroclinic generation due to hydrodynamic pressure is zero, and thus only hydrostatic pressure effects are treated. This is the Boussinesq approximation. In this case, Eq. (3) becomes (without the $\tilde{\cdot}$ notation)

$$\frac{D\boldsymbol{\gamma}}{Dt} = \frac{1}{R^2}\boldsymbol{\gamma}\cdot(\nabla\boldsymbol{u}) - 2\theta\hat{\boldsymbol{n}} \times \frac{\boldsymbol{g}}{||\boldsymbol{g}||}. \tag{8}$$

This is the governing equation for the evolution of the vortex sheet strength in three-dimensional flow. We will show, in Section 3, how the very construction of the numerical method automatically satisfies the vortex stretching term in this equation.

2.1. Velocity

The fluid velocity must be defined on the vortex sheet in order to convect it through the domain. The formula governing the motion of a fluid by the action of a vortex sheet is

$$\boldsymbol{u}(\boldsymbol{x},t) = \frac{1}{4\pi}\int_S \frac{\boldsymbol{\gamma}(\boldsymbol{S},t)\times(\boldsymbol{x}-\boldsymbol{S})}{|\boldsymbol{x}-\boldsymbol{S}|^3}\,dS. \tag{9}$$

An alternative method to compute the velocity uses the definition of vorticity ($\boldsymbol{\omega} = \nabla \times \boldsymbol{u}$), the vector identity

$$\nabla^2\boldsymbol{A} = \nabla(\nabla\cdot\boldsymbol{A}) - \nabla\times\nabla\times\boldsymbol{A}, \tag{10}$$

and the assumption of incompressibility ($\nabla\cdot\boldsymbol{u} = 0$), to show that

$$\nabla^2\boldsymbol{u} = -\nabla\times\boldsymbol{\omega}. \tag{11}$$

This formulation is more amenable to the combined Lagrangian–Eulerian solution method described in Section 3.1.

3. Numerical method

As is common in three-dimensional front-tracking schemes, the front is discretized into flat triangles, each defined by its connectivity to three Lagrangian nodes. In the present method, the edges of each triangular element p store scalar-valued circulations $\Gamma_{p,1\to 3}$. The sum of the circulations multiplied by their respective edge vectors $\Delta \boldsymbol{l}_{p,1\to 3}$ uniquely defines the vortex sheet strength $\boldsymbol{\gamma}_p$ of each element according to

$$\boldsymbol{\gamma}_p = \frac{1}{a_p}\sum_{i=1}^{3}\Gamma_{p,i}\Delta\boldsymbol{l}_{p,i}, \tag{12}$$

where a_p is the element area.

One Euler time step consists of the following substeps: interpolate element vorticity onto a grid, solve for velocity, interpolate velocity back onto mesh nodes, move mesh nodes, generate baroclinic vorticity on each element, remesh to maintain element quality and density. Time integration for all simulations in the present work is carried out by an explicit second-order Runge–Kutta method, specifically Heun's method. In this multistep method, the remeshing is done only once per time step: at the end of the forward integration and before output. The method uses an adaptive step size corresponding to a Courant number of at least unity

$$\frac{||\boldsymbol{u}||_{\max}\Delta t}{\Delta x} \geqslant 1. \tag{13}$$

3.1. Velocity calculation

The velocity of the computational nodes is calculated from the vorticity field using Eq. (11). The vorticity field is created from the current vortex sheet geometry and element strengths according to

$$\boldsymbol{\omega}(\boldsymbol{x}) = \sum_{p=1}^{N} a_p \gamma_p \, \delta(\boldsymbol{x} - \boldsymbol{x}_p), \tag{14}$$

where δ is a regularized delta function.

In the present work, a three-dimensional version of Peskin's function [36] is used as the particle-grid operator δ. This version is simply a tensor product of three one-dimensional Peskin functions, and thus has a strictly positive (though rectangular in two and three dimensions), support.

$$\delta_\varepsilon(x) = \begin{cases} \frac{1}{2\varepsilon}\left[1 + \cos\left(\frac{\pi x}{\varepsilon}\right)\right] & : \quad |x| \leqslant \varepsilon \\ 0 & : \quad |x| > \varepsilon \end{cases}, \tag{15}$$

$$\delta(\boldsymbol{x} - \boldsymbol{x}(s)) = \prod_i \delta_\varepsilon(x_i - x_i(s)). \tag{16}$$

The function is C^∞ continuous and is second-order accurate when the kernel width ε takes on values $[1, 1.5, 2, \ldots]\Delta x$. While the Peskin function is more costly to implement and can have a larger support than other popular kernels, it offers benefits related to solution smoothness, long-time suppression of grid instabilities, and better conservation of flow invariants. More details appear in [37].

The velocity field is computed by solving Eq. (11) once for each of the three velocity components on a temporary, regular grid with boundary conditions arising from the type of domain boundary chosen (open, periodic, or slip wall). The right-hand-side of this equation is computed using second-order centered and one-sided derivatives of the vorticity field from (14). Modern fast Poisson solvers, which can use Fast Fourier Transforms or multigrid methods, can solve this equation in $\mathcal{O}(M \log_2 M)$ or better time, where M is the number of cells in the discretized volume. The HW3CRT solver from Fishpack [38] is used in the present method.

Upon evaluation of the velocity, the evolution of the marker node positions is determined by integrating

$$\frac{\mathrm{d}\boldsymbol{x}_p}{\mathrm{d}t} = \boldsymbol{u}_p, \tag{17}$$

where $\boldsymbol{u}_p$ is interpolated from the grid velocity using

$$\boldsymbol{u}_p(\boldsymbol{x}_p) = \sum_{j=1}^{M} \boldsymbol{u}_j \, \delta(\boldsymbol{x}_p - \boldsymbol{x}_j) \tag{18}$$

and the same kernel used in (14).

3.2. Vorticity update

Because the vortex sheet strength of each element is stored as circulations on the triangle edges, and these circulations are unchanged during the convection step, the vortex stretching term is satisfied automatically and exactly.

The other term in the vortex sheet strength evolution Eq. (8) governs the strength change due to baroclinic generation. Updating the edge circulations of the elements reduces to two simple steps. The first is to integrate

$$\frac{\mathrm{D}\gamma_p}{\mathrm{D}t} = -2\,\theta\,\hat{\boldsymbol{n}}_p \times \frac{\boldsymbol{g}}{||\boldsymbol{g}||} \tag{19}$$

forward in time within the convection step, where $\hat{\boldsymbol{n}}_p$ is constant on each triangular element and calculated using the cross-product of two edge vectors. The second step is to convert the change in element vortex sheet strength to a change in the circulations on the element edges. This is done by solving a set of equations equivalent to the inverse of (12). The resulting change in edge circulations is added to the existing circulations on that element's edges.

3.3. Remeshing

In order to maintain constant mesh resolution and smoothness in the presence of strain, the sheet undergoes local remeshing once every time step. This remeshing consists of two steps: splitting edges to maintain mesh resolution in areas of extensional strain and merging nodes to simplify mesh geometry and coalesce layers. Without this remeshing, elements would elongate beyond the capacity of the VIC grid to resolve them smoothly, and elements would collect into zones with many thin, redundant triangles and parallel edges.

At every time step, all triangle edges whose length exceeds $0.8\Delta x$ are flagged for splitting. This step consists of creating a new node at the midpoint of each long edge and then performing the following operations for every triangle that shares that edge: (a) determine the vortex sheet strength of the original triangular element, (b) logically split the original element into two child elements using the new node and (c) set the circulations on the two child elements using the vortex sheet strength of the parent element and the areas and edge vectors of the child elements according to the procedure described in Section 3.2. Because the triangle area and normal stay constant throughout this process, circulation is exactly conserved. Note that this method allows *local sheet* refinement, unlike schemes that use filaments to represent sheets, and allows efficient refinement in *any* sheet-tangent direction, unlike quadrilateral-based remeshing schemes which are not efficient along their diagonal. Local curvature can also be used to locate the new node [33,37]; this does not affect the conservation properties of the splitting routine.

Were this the only remeshing process, the effect of compressional strain along either of the sheet tangential axes would cause most elements to become elongated and very thin. A merging process combines nodes that approach to within a threshold distance of each other (normally $0.2\Delta x$). Nodes may be merged only with local nodes within the same sheet (manifold or sheet merge), or with any close nodes, regardless of connectivity changes (full merge). The merging procedure is composed of the following steps: (a) identify via a uniform, binned, node search strategy node pairs within the threshold distance, (b) identify any elements that contain both nodes in any node pair, (c) relocate the circulation from those elements' edges onto the shared edges of their neighboring elements, (d) merge the nodes into one node at their midpoint, (e) delete the elements identified in step (b), and (f) merge any element pairs that, after the merge, are composed of the same three nodes. Because the scheme reorients the tangents of participating triangular elements, and the discretization allows only in-plane vortex sheet strength, the scheme does not conserve total circulation. The amount of circulation removed is typically very small, and the scheme behaves as a subgrid-dissipation step [37] in the same vein as hairpin removal techniques [20].

No smoothing, "fairing," or feature suppression is done on the mesh (as in [3,29]), nor is any smoothing done on the strengths of the elements (as is done to suppress instabilities in [25]). Because of this, details the size of the smallest unstable wavelength will spontaneously appear, making resolution convergence tests with the same interpolation kernel impossible. Regardless, runs at different resolutions will retain very similar overall behavior, though the small scales may appear different. In addition, simulations with identical non-dimensional regularization produce identical results. Component and full-system validation tests of the method appear in [37].

4. Results

The interaction between a vortex ring and a density interface is a complex test for three-dimensional vortex sheet methods. Some examples of this problem include the interaction of a ship wake with a thermocline, the collision of a thermal with an inversion layer, and the interaction of vorticity with a flame front.

Previous experimental studies of vortex ring interactions with sharp density interfaces appear in Linden [39] (turbulent vortex rings) and Dahm et al. [40] (laminar rings). Numerical solutions from Tryggvason [41], Dahm et al. [40] and Tryggvason et al. [42] use both two-dimensional and axisymmetric vortex sheet methods. Results from a three-dimensional vortex sheet simulation appear in Tryggvason et al. [42], but no details are presented. Related research treats the interface as a free surface instead of a finite density gradient [41–45], but this typically requires a boundary element integral solution, which is not included in the present implementation. Marcus and Bell [46] present results from axisymmetric Navier–Stokes calculations for the non-Boussinesq case. A three-dimensional vortex particle method was used by Liu [47,48] to study the normal impact of a vortex ring into a wall. Other studies present physical and numerical experiments of the wall interaction case [49–53].

This problem can be described by four parameters: the diameter of the vortex ring D, its circulation Γ, the Boussinesq coefficient θ, and the regularization length scale δ. Holding the core function constant, the four remaining quantities allow two similarity parameters: the non-dimensional regularization $\delta^* = \delta/D$ and the non-dimensional Boussinesq coefficient

$$\theta^* = \frac{A}{Fr} = \frac{AD^3g}{\Gamma^2}. \tag{20}$$

Other variables have been normalized as follows: time $t^* = t\Gamma/D^2$, length $x^* = x/D$, velocity $u^* = uD/\Gamma$ and vorticity $\omega^* = \omega D^2/\Gamma$.

The problem involves a stable density interface extending to infinity in the horizontal dimensions (x and y), but for the cases presented, an open domain with sufficient size is used. The computational domain thus has bounds [−3:3] [−3:3] [−3:3] and free-space boundary conditions in all directions. The radially-symmetric Peskin function is used for all particle-grid operations, and the filter radius is $\varepsilon = 4$, giving $\delta_{\text{Peskin}} = 4\Delta x$. The regularization length scale for the subsequent runs is $\delta^* = 0.2$, which corresponds to a grid resolution of $\Delta x = 1/20$. Time steps were in the range $0.05 < \Delta t < 0.06$.

The lack of a stabilizing influence such as viscosity or surface smoothing in inviscid regularized vortex sheet motion allows instabilities with wavelengths greater than some multiple of the regularization length to grow unchecked. This is especially noticeable when simulating vortex rings, as a grid- induced instability with azimuthal wavenumber $k = 4$ tends to distort an initially circular ring into a square. This was first seen in vortex filament studies of vortex rings [11]. Results from Section 4.1 are presented here in order to demonstrate this distortion in a vortex sheet method. Fig. 1 shows the three-dimensional computational surface and the ring-plane peak vorticity.

The numerical experiments of Dahm et al. [40] were of the axisymmetric or planar type, and thus allowed no azimuthal instability, despite being regularized inviscid methods. The computational boundaries could then be set much closer to the active areas of the flow. The only effects of reducing the horizontal domain from 8 to 4 diameters were a subtle thinning of the resultant sheet structure in the horizontal direction and a change in the elevation of the density layer at the boundaries. The domain size for the present simulations (6D) was cho-

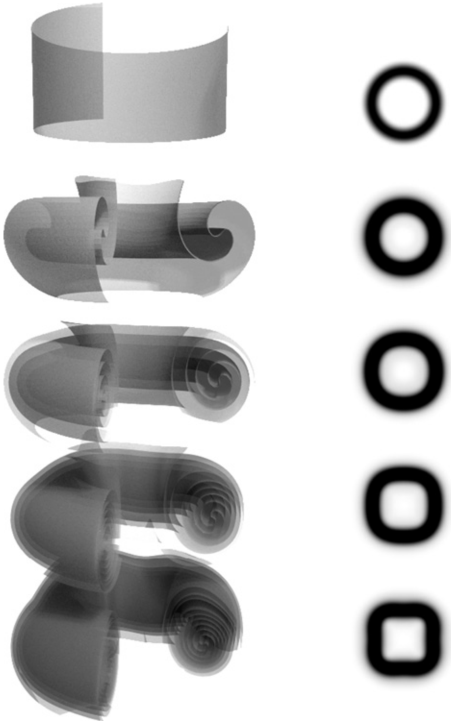

Fig. 1. Interface positions (left) and x–y plane $|\omega|$ column maxima (right) for case with $\theta^* = 0.0, t^* = [0, 2, 4, 6, 8], \delta^* = 0.2$, for the images on the right $|\omega^*| > 10$ is solid.

sen as a compromise between the growth rate of the $k = 4$ instability seen in Fig. 1 and the available computational resources.

4.1. No baroclinic generation

For the sake of comparison with subsequent simulations, and to provide a control of the simulation parameters, a case is run with a passive interface ($\theta^* = 0$). The laminar vortex ring in these simulations formed from an initially cylindrical tube $D/2$ long with uniform circumferential vortex sheet strength $\gamma = 2\hat{e}_\theta$. The sheet dynamics and vorticity field corresponding to this case can be seen in Fig. 2. The initially cylindrical ring rolls up into a thick-cored vortex ring as early as $t^* = 2$ and the vorticity distribution across the ring minor radius is similar to that of thick-cored rings: never symmetric and always favoring the inner side.

For the given regularization length scale, it takes about three turns for most of the vorticity in the cylinder to roll up into a smooth vortex core. The distribution of vorticity inside this core, seen in Fig. 2, resembles a Gaussian [54,55], which is also demonstrated in ([37], Fig. 4.4). Numerical comparisons to Fraenkel's thin-cored [56] or Norbury's family of thick-cored vortex rings [57] were not made.

Several parameters from this test appear in Fig. 3. First, the vertical extent of the computational elements indicates the maximum penetration of the vortex ring into the density interface. It is not surprising that the lowest point on the interface accelerates downward and continues at a nearly constant rate, as it is pushed by a constant-strength vortex ring. The highest point on the mesh in this case corresponds to the remainder of the horizontal interface that is not entrained and remains at its initial altitude. Next, the vertical velocity of the center of vorticity shows a stable but oscillating vortex ring velocity of $u_z^* \simeq 0.4$. Applying Helmholtz's equation for the velocity of a thin-cored vortex ring

$$U = \frac{\Gamma}{4\pi R}\left[\log\frac{8R}{r} - \frac{1}{4}\right], \tag{21}$$

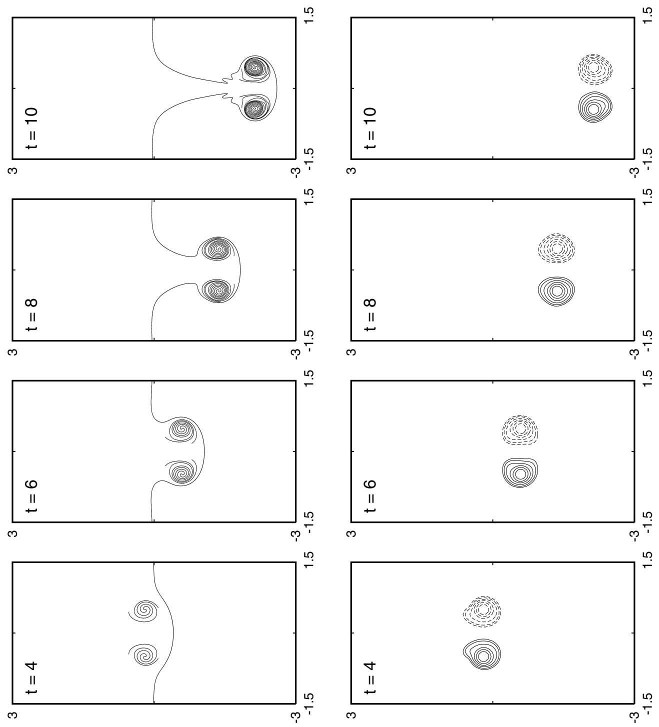

Fig. 2. Centerline slices through vortex sheet (left) and vorticity (right) for $\theta^* = 0, \delta^* = 0.2$ contours are at $\omega^* = \pm 0.25, 0.5, 1, 2, 4, 8$.

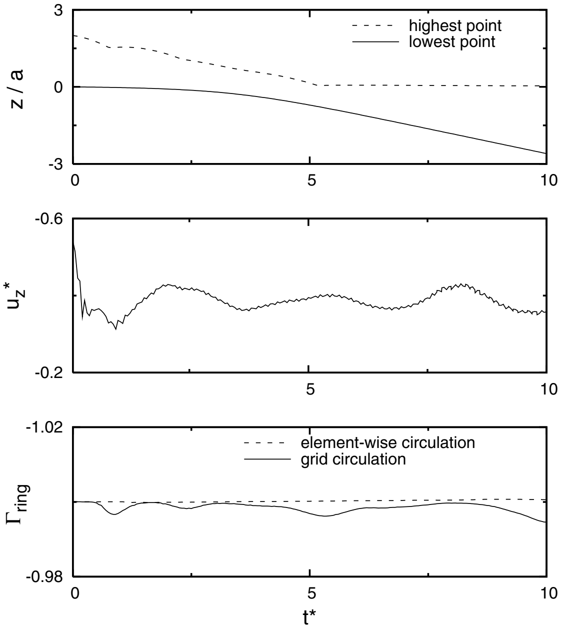

Fig. 3. Vertical bounds, vertical speed of center of vorticity, and total circumferential circulation for vortex ring impacting a zero-strength one-layer interface, $\delta^* = 0.2$.

returns a core (minor) radius of $r \simeq 0.25$, which corresponds to the radius at which the vorticity has dropped to 10% of its peak. The vortex ring maintains nearly constant circulation throughout the simulation. The total circumferential circulation is not expected to stay constant for subsequent cases with $\theta^* > 0$, as the downward distortion of the density interface should create counter-circulation.

4.2. Thin interface

In the following simulations, the same vortex ring from the above non-baroclinic case is ejected perpendicular to a single regularized density discontinuity of uniform strength. The strength of this discontinuity is measured by the Boussinesq coefficient, which takes on values $\theta^* = [0.03, 0.1, 0.3, 1.0, 3.0]$. Similar simulations of oblique impacts are presented in [37].

These are the three-dimensional analogues of simulations in Dahm et al. [40] that used a two-dimensional vortex pair formed from a circular vortex sheet. Previous studies [58,59] show that those conditions result in a thick-cored vortex pair while the present method creates rings with a “thin” core.

Cross-sections in the x–z plane of both the computational surface and the normal vorticity ω_y appear in Figs. 4–9. From this series of images, the effect of the density interface on the vortex ring can be easily seen. In the case of the weakest density jump ($\theta^* = 0.03$, Fig. 4), the vortex ring behaves nearly identically to the non-baroclinic case in Fig. 2, except for the generation of weak oppositely-signed vorticity along the walls of the cavity pushed out by the vortex ring. The final frame in that series shows that a small amount of the vortex ring outer layer is finally peeled off by that counter-signed vorticity. Using an argument based on energy balance, it can be reasoned that had the simulation run longer, the vortex ring would eventually slow and reverse its downward motion.

The $\theta^* = 0.1$ case in Fig. 5, having a density interface three times stronger than the weakest case, exhibits significantly increased counter-rotating vorticity along the cavity walls. This causes vorticity from the vortex ring to be stripped away earlier than the previous case (by $t^* = 8$) and also causes the highest rebound of any of the cases tested. It is clear that this high rebound (seen at $t^* = 10$) is allowed because the amount of counter-vorticity is significant but not so large that it disallows the main vortex ring from penetrating at all. Thus, the counter-rotating vortex ring is free to travel upwards, not significantly hindered by the primary vortex ring.

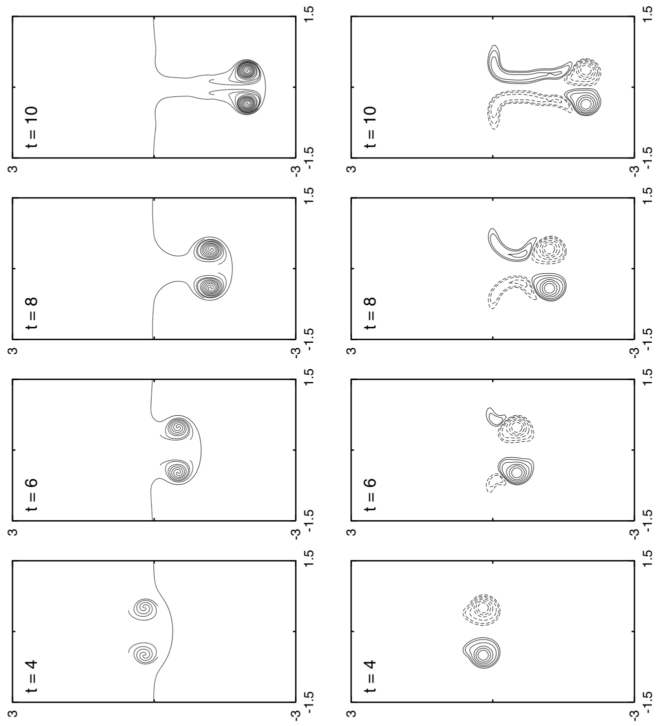

Fig. 4. Centerline slices through vortex sheet (left) and vorticity (right) for $\theta^* = 0.03, \delta^* = 0.2$ contours are at $\omega^* = \pm 0.25, 0.5, 1, 2, 4, 8$.

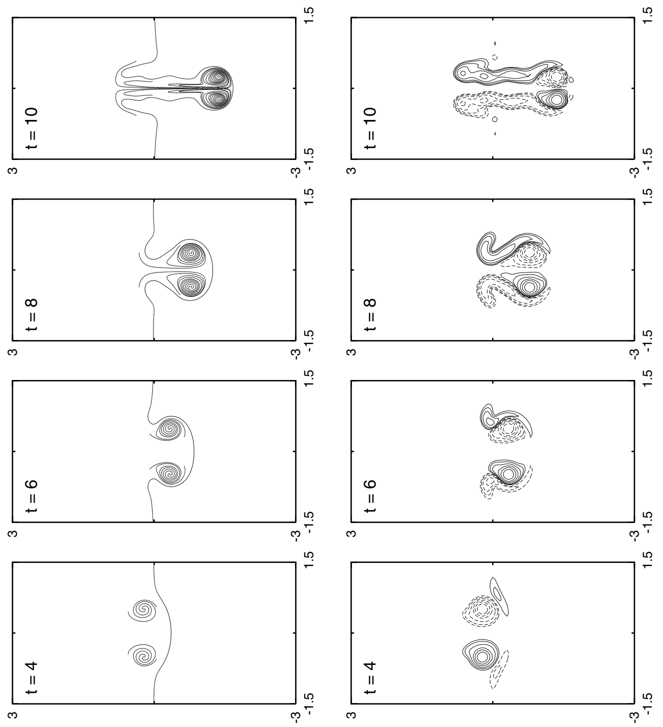

Fig. 5. Centerline slices through vortex sheet (left) and vorticity (right) for $\theta^* = 0.1, \delta^* = 0.2$ contours are at $\omega^* = \pm 0.25, 0.5, 1, 2, 4, 8$.

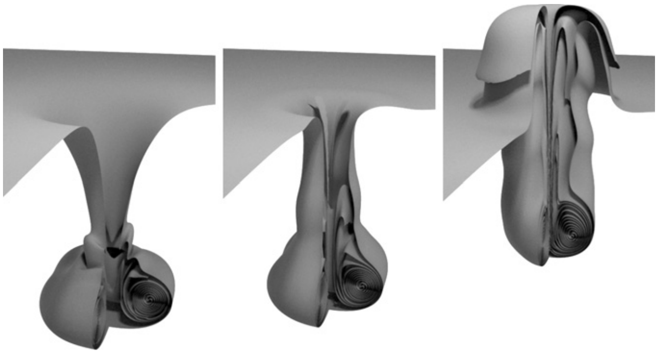

Fig. 6. Rendered vortex sheet surface at $t^* = 10$ for $\theta^* = [0.0, 0.03, 0.1]$, $\delta^* = 0.2$.

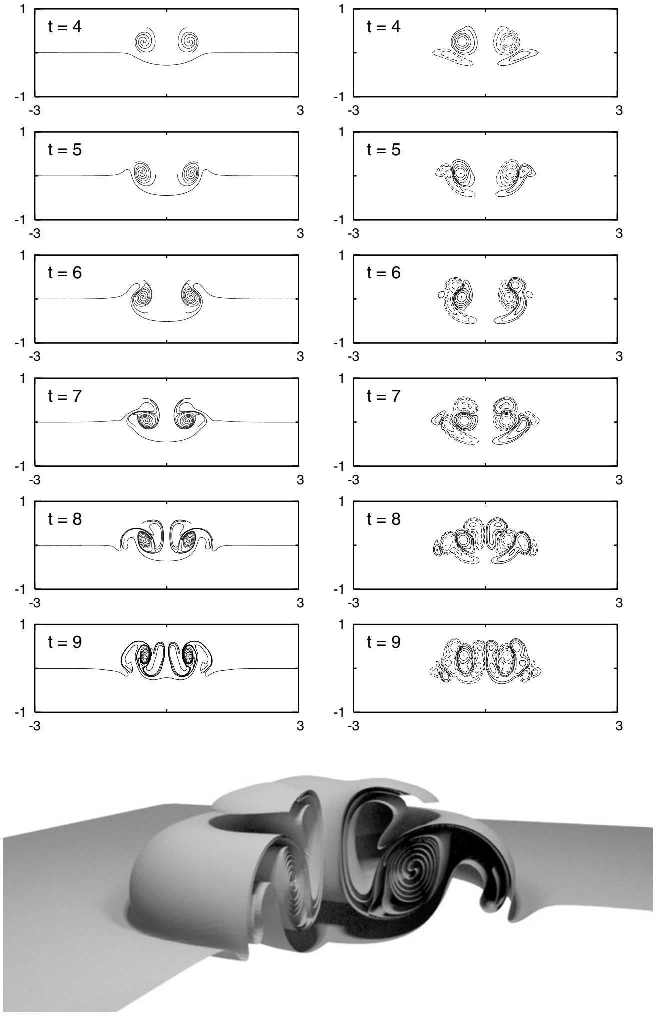

Fig. 7. Centerline slices through vortex sheet (left) and vorticity (right) for $\theta^* = 0.3$, $\delta^* = 0.2$, contours are at $\omega^* = \pm 0.5, 1, 2, 4, 8, 16$, rendering is at $t^* = 8$.

The backflowing jet is also unstable to waves of the Kelvin–Helmholtz style, though a complete roll is not observed. This is very similar to the behavior in the experiments and numerical results in ([40], Figs. 5, 9, 14).

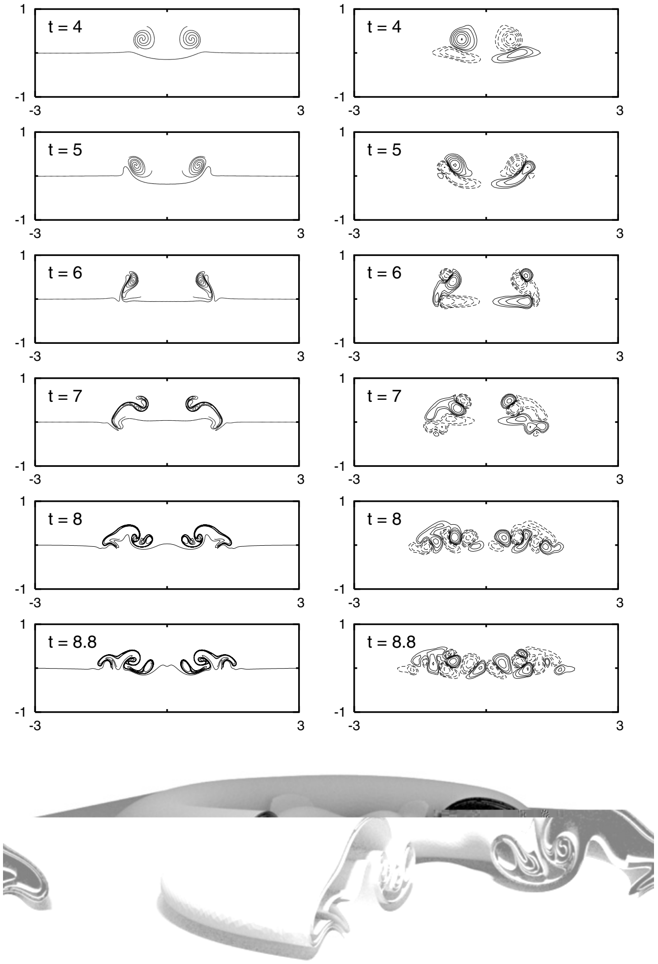

Fig. 8. Centerline slices through vortex sheet (left) and vorticity (right) for $\theta^* = 1.0$, $\delta^* = 0.2$, contours are at $\omega^* = \pm 0.5, 1, 2, 4, 8, 16$, rendering is at $t^* = 8$.

Unlike the previous cases with relatively weak density layers, when $\theta^* = 0.3$ the vortex ring does not penetrate the interface (Fig. 7). Instead, it pulls together portions of the density interface to form a second vortex ring with smaller circulation and opposite sign. The second ring, being weaker, does little to disturb the primary vortex ring from its stable position just above the initial level of the density layer. The primary vortex ring then proceeds to gather a second counter-rotating vortex ring from $t^* = 6 \rightarrow 8$ while the first continues around the top of, and into the middle of the primary ring. All of this oppositely-signed vorticity slowly weakens the primary vortex and concurrently creates new vortex rings farther from the axis, each with circulation opposite the previous ring. This repeating creation of vortex rings is similar in nature to the repeated pairings encountered in simulations of viscous vortex dipoles impinging on a no-slip wall [60]. The dynamics of this case are similar to the experiments in ([40], Figs. 4, 7, 11, 17).

The behavior of the $\theta^* = 1.0$ and $\theta^* = 3.0$ cases, appearing in Figs. 8 and 9, are remarkably similar, though different in degree. These two cases with the strongest density interface (still using the Boussinesq limit, of course) follow nearly the same progression as the next-weaker case ($\theta^* = 0.3$) in which the impinging primary vortex effectively ‘‘bounces’’ off of the density interface, tearing off and pairing with a counter-rotating vortex ring built from the density interface. These new rings in turn distort the surface and create more new rings with circulation opposite to themselves. By $t^* = 8$, the $\theta^* = 1.0$ case has no fewer than six rings and the $\theta^* = 3.0$

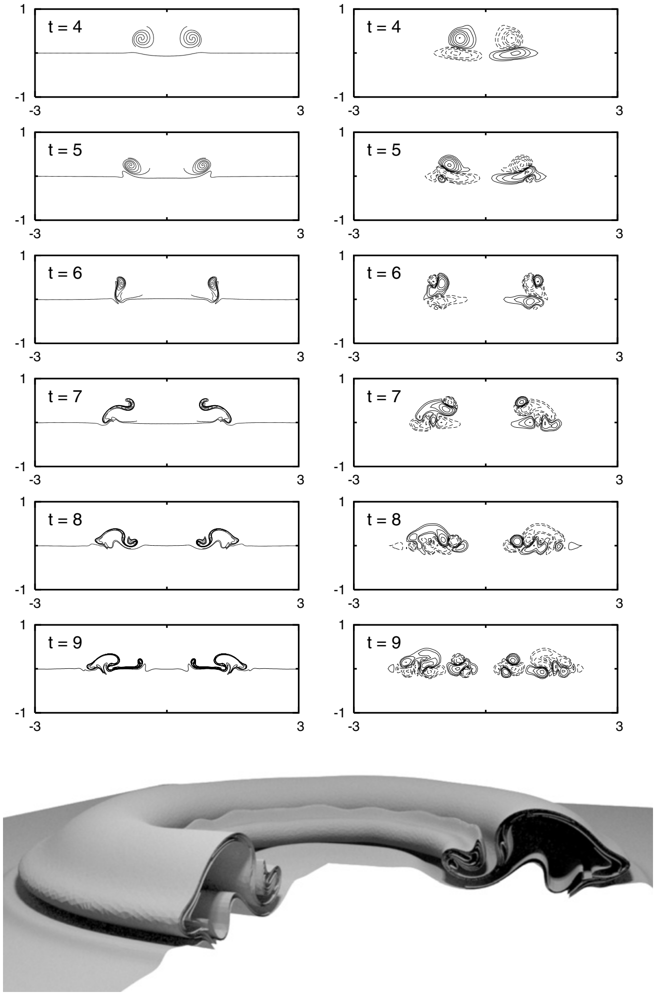

Fig. 9. Centerline slices through vortex sheet (left) and vorticity (right) for $\theta^* = 3.0$, $\delta^* = 0.2$, contours are at $\omega^* = \pm 0.5, 1, 2, 4, 8, 16$, rendering is at $t^* = 8$.

case has nearly ten. With a stronger density interface, these rings are formed at larger radii and are wound up more tightly; though the overall dynamics are similar. The resulting motions bear remarkable similarity to the experiments of Walker et al. ([49], Fig. 9) and Dahm et al. ([40], Fig. 8, 18, 26, 27, and 33).

A curious instability appears in the latest stages of the $\theta^* = 3.0$ case. It manifests as an azimuthal perturbation of the original vortex ring, seen in Fig. 10 and identifiable in the time series in Fig. 9. This Crow-type instability has been attributed to rapid distortion of the secondary vortex ring by the strain induced by the strong and more stable primary vortex ring [61,52]. The same instability may be responsible for the rapid onset of turbulence in high Reynolds number jet flow [62]. It is unclear whether any of the nearby secondary vortex rings are responsible for this. The wavelength at $t^* = 9$ is $\lambda \approx 0.5D$, or $\lambda \approx 2.5\ \delta_{\mathrm{Peskin}}$, which is much smaller than the most-perturbed wavelength in the Kelvin–Helmholtz instability ($\lambda \approx 7\ \delta_{\mathrm{Peskin}}$) but similar to that observed in experiments of a sphere impacting a wall [53] (where $\lambda \approx 0.4D$). The secondary instabilities that were observed in the viscous vortex particle simulations in Liu [47], however, were the result of an initially perturbed vortex ring.

While this instability appears in experiments [40,49,52,53,63] and viscous simulations [50,51,53] of vortex ring impacts with a wall, it is not known to have been demonstrated for an inviscid vortex ring impacting on a density interface. The reason that an inviscid simulation can exhibit behavior only previously seen in vis-

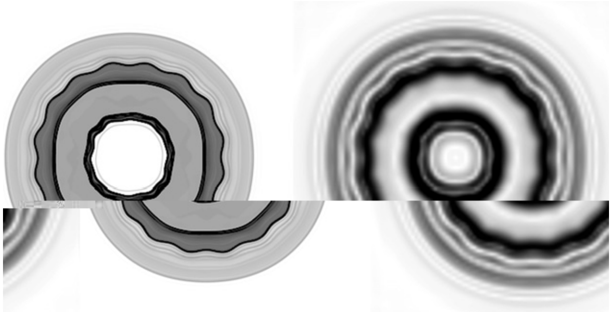

Fig. 10. Vortex sheet (left) and vorticity magnitude (right) for $\theta^* = 3.0, t^* = 9, x$–$y$ plane, $\delta^* = 0.2, |\omega^*| > 10$ is black; showing onset of Crow-type instability normally associated with impact of viscous vortex ring on a wall.

cous flow is that, like a no-slip wall, the inviscid baroclinic interface can generate counter-vorticity that can be pulled away from the "wall" and eventually become enveloped in the primary vortex ring, thus initiating the azimuthal instability. Theory and details concerning this instability can be found in Swearingen et al. [51]. The interaction of a vortex and a contaminated free surface also exhibit this type of behavior [42].

The penetration distance of the vortex sheet appears in Fig. 11. Unlike the results in Dahm et al. [40], the penetration distance in the present work is not measured along the vortex ring axis, but instead represents the minimum vertical node location of the entire computational surface. Additionally, to quantify any significant rebound, the maximum vertical node location was also tracked. This figure plainly shows the transition in penetration distance that occurs between $\theta^* = 0.1$ and $\theta^* = 0.3$. Also obvious is that the range of values from minimum to maximum position is narrower for stronger stratification. The only real surprise concerns the larger rebound of the $\theta^* = 0.1$ and $\theta^* = 0.3$ cases. As mentioned earlier, this large and early rebound is due to the the upward-moving oppositely-signed vorticity generated on the inside of the cavity and the inability of the primary vortex ring to suppress its rebound. It is also likely that the $\theta^* = 0.03$ case would have rebounded similarly had it run longer. From the maximum penetration vs. θ^* data in Fig. 12, it is clear that the initial downward motion of the interface scales logarithmically with θ^*. This representation of the data also illustrates the same conclusion drawn from ([40], Fig. 20): that there is a sharp transition from strong dependence on θ^* to relatively weak dependence.

The center of vorticity for each run was tracked and the results appear in Fig. 13. Note that for cases with multiple vortex rings, this is not the center of the strongest ring, but simply the center of mean magnitude in the radial and vertical directions. In all cases with $\theta^* \leqslant 0.1$ the primary vortex ring penetrated the surface and

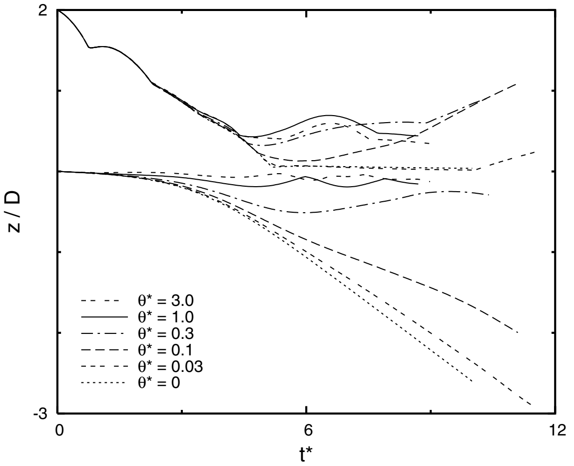

Fig. 11. Vertical bounds for normal impact cases, one-layer interface with various $\theta^*, \delta^* = 0.2$.

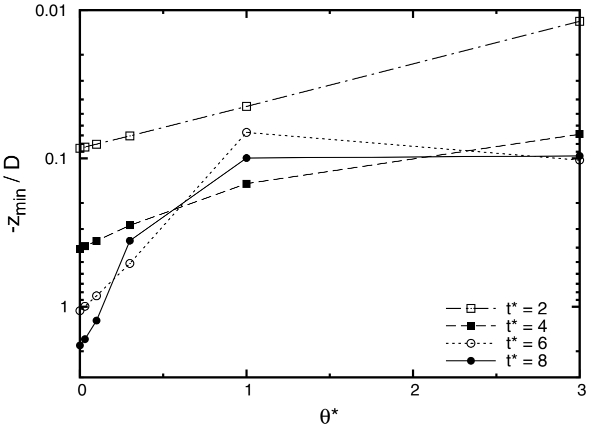

Fig. 12. Maximum penetration depth for normal impact cases, one-layer interface with various $\theta^*, \delta^* = 0.2$.

did not begin its return by the time the simulation ended. The $\theta^* = 0.1$ case, being the most strongly-stratified case that still allowed the vortex ring to fully penetrate, also exhibited the greatest reduction in vortex ring radius. In the cases with $\theta^* \geqslant 0.3$ the primary ring looped around nearby counter-rotating vortex rings at near the level of the initial density interface. The single loops taken by the center of vorticity in the $\theta^* = 1$ and $\theta^* = 3$ cases correspond well to the trajectory of the primary ring from Walker et al. ([49], Fig. 11) for $Re > 2000$.

The kinetic energy, enstrophy, and total circumferential circulation all appear in Fig. 14. For the most part, the performance is as expected: larger θ^* translates to greater enstrophy ε and faster reduction of circulation Γ. The oscillations of all three flow quantities also increase in frequency for larger θ^*. The kinetic energy, though,

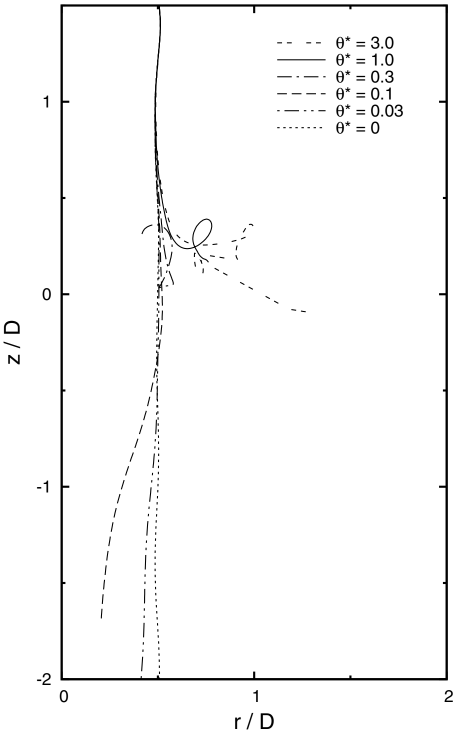

Fig. 13. Position of center of vorticity of vortex ring for normal impact cases, one-layer interface with various $\theta^*, \delta^* = 0.2$.

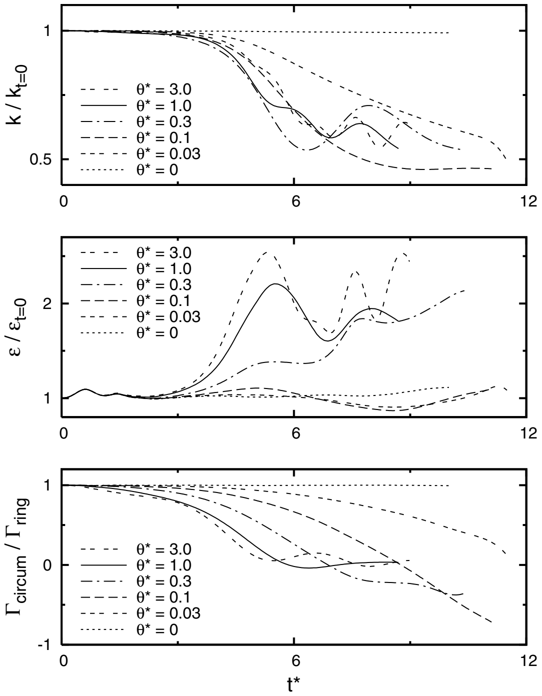

Fig. 14. Specific kinetic energy, enstrophy, and total circumferential circulation for normal impact cases, one-layer interface with various $\theta^*, \delta^* = 0.2$.

shows more interesting behavior. The drop in kinetic energy is most rapid for the $\theta^* = 0.3$ case, and less rapid as θ^* strays from 0.3. This is another indication that $\theta^* = 0.3$ represents a transitional case between a stronger primary vortex ring and a stronger density interface. When either of the two greatly overpowers the other, there is little incentive to dissipate energy: the vortex would effortlessly pass through the interface or the interface would act as a wall and influence the vortex to grow radially before it gets close enough to pull any vorticity away.

Computational requirements for the $\theta^* = 0.1$ case are representative of the rest of the simulations, and are as follows. The number of elements ranged from 125,204 to 392,571, which required from 14.05 to 45.58 s on a 1.83 GHz AMD Athlon XP to interpolate vorticity onto the grid. One VIC solution on the 120^3 grid took from 14.67 to 208.47 s, but included a direct summation calculation for the free-space boundary conditions.

To validate the implementation of the method and to see how well the invisicd model captures the motion of real fluids, when the viscosity is low, the head-on collision of the ring for the $\theta^* = 0.1, 0.3$ cases (Figs. 5 and 7) was compared to simulations using the full Navier–Stokes equations in an axisymmetric domain. The method used is an axisymmetric version of the front-tracking method of Unverdi and Tryggvason [34]. The code has been used to study several problems and a detailed description and validations can be found in Han and Tryggvason [64,65]. The simulations were done in a domain of 3 by 6 ring diameters D, resolved by a 256 by 512 uniform grid. The initial conditions were exactly the same as used for the fully three-dimensional inviscid simulations. The viscosity was selected such that $\Delta\rho g D^3/(\mu\Gamma) = 200$.

Figs. 15 and 16 show the fluid interface and the vorticity at four times for the two cases. In each frame the results from the inviscid simulations are shown on one side and the axisymmetric Navier–Stokes results are shown on the other. The initial vortex sheet is included for the inviscid simulations, but only the density interface is shown for the Navier–Stokes results. Dashed and solid contour lines are used for vorticity of the opposite sign. Overall the solution is similar for the inviscid and the full Navier–Stokes cases, particularly at early times. At later times the differences increase, as expected, when viscous diffusion leads to mutual annihilation of vorticity of the opposite sign in the full Navier–Stokes case. The maximum depths of the fluid interface for both cases, as computed using the inviscid method and the Navier–Stokes solver, are compared in Fig. 17.

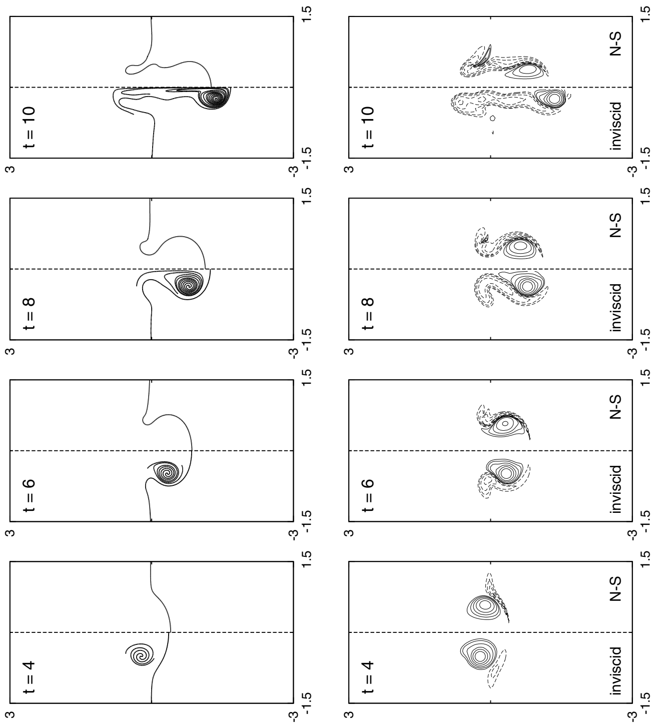

Fig. 15. Centerline slices through vortex sheet (left) and vorticity (right) for $\theta^* = 0.1$, comparing present inviscid and viscous Navier–Stokes simulations; contours are at $\omega^* = \pm 0.25, 0.5, 1, 2, 4, 8$.

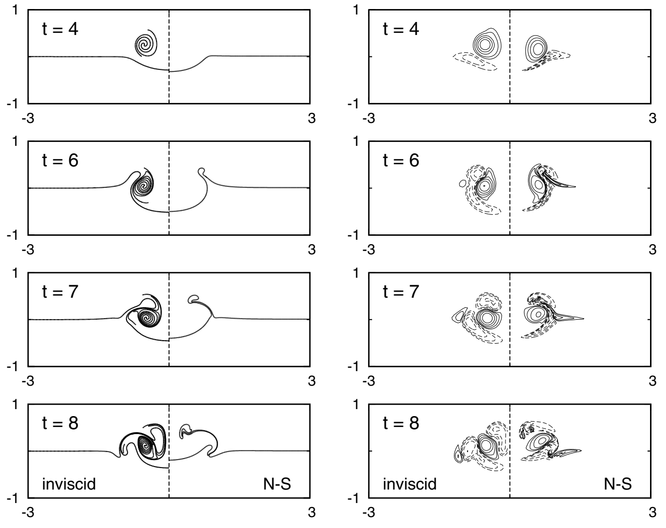

Fig. 16. Centerline slices through vortex sheet (left) and vorticity (right) for $\theta^* = 0.3$, comparing present inviscid and viscous Navier–Stokes simulations; contours are at $\omega^* = \pm 0.5, 1, 2, 4, 8, 16$.

Obviously the agreement is good for the early times, although the results diverge at later times when the effect of the viscosity become important. Simulations run with higher viscosities showed the solutions diverging earlier as the viscosity is increases, as one would expect.

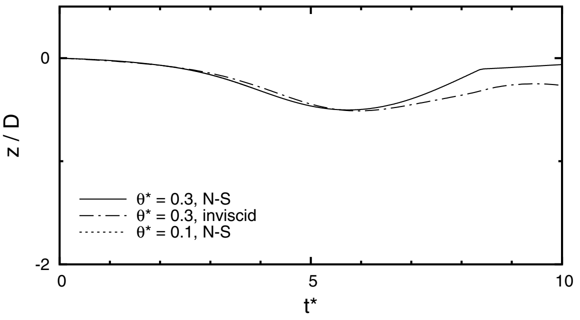

4.3. Thick interface

Because most weak density interfaces in nature and technology are not sharp such as those in the preceding sections, additional simulations of a vortex ring impact with a thick density interface were performed. Previous experiments [40] have addressed the dynamics of a vortex ring impact with a thick interface, and vortex methods have been shown to be able to simulate thick vortex sheets in two [66,67] and three dimensions [30,31], though no method has demonstrated a vortex ring impact into a thick density interface.

The inclusion of sheet thickness into the similarity assumptions generates a new similarity parameter, the non-dimensional sheet thickness σ^*, given as the characteristic sheet thickness σ (one standard deviation in the case of a Gaussian) divided by the vortex ring diameter D, or $\sigma^* = \sigma/D$. The only case investigated in the current work has $\sigma^* = 0.1$.

The value of the density gradient through the interface follows a Gaussian profile, that being the solution to the stationary one-dimensional diffusion equation in the normal direction. The thick sheet is discretized into five initially-coplanar layers, each with a fraction of the total Boussinesq coefficient θ^* according to a Gaussian function. The top and bottom sheets are separated by four standard deviations that cover two regularization lengths, or $\sigma^* = \delta^*/2$. The summation of the Peskin functions for these five layers does not reproduce a Gaussian profile any better than one single Peskin function does, but was intended to reproduce a regularized thick layer in the same manner as previous studies [30]. It is assumed that inaccuracies will become present in these simulations when the distance between two sheets exceeds the regularization length.

A simulation was run with the same vortex ring as the previous sections and the aforementioned thick interface with total Boussinesq coefficient $\theta^* = 1.0$, non-dimensional sheet thickness $\sigma^* = 0.1$, and regularization length scale $\delta^* = 0.2$. Cross-sections of the thick interface and corresponding vorticity fields appear in Fig. 18. The most notable difference between the computational surface cross-sections concerns the compression of the density layers into a single high-gradient region in the central area inside of the primary vortex ring. The counter-rotating vortex ring also seems to have a higher peak vorticity in the single-layer case, which is understandable as the multiple-layer case would have spread the generated vorticity over a larger volume. Again it should be noted the good agreement between these numerical results and previous experiments [40].

The motion of the center of vorticity, shown in Fig. 19, differs only in the late stages of the simulation. The data clearly show that the secondary vorticity generated from the thick interface forces the primary vortex ring to spin over upon itself more quickly than for the single-layer case. This is presumably due to earlier generation of vorticity on the uppermost layers of the thick interface influencing the primary vortex ring.

The maximum penetration into the thick interface is compared to the single-layer case in Fig. 20. In the single-layer case the vortex sheet confines itself to a smaller vertical extent, and it is reasonable to expect it to remain this way beyond the end of the simulation.

Thickening the density interface affects the character of the change in kinetic energy and enstrophy, but not the circumferential circulation, all illustrated in Fig. 20. The kinetic energy and enstrophy for the case with a single density layer oscillate at they progress, while the thick interface simulation exhibits more uniform behavior. The smaller density gradient in the latter case must allow for a more stable environment for the

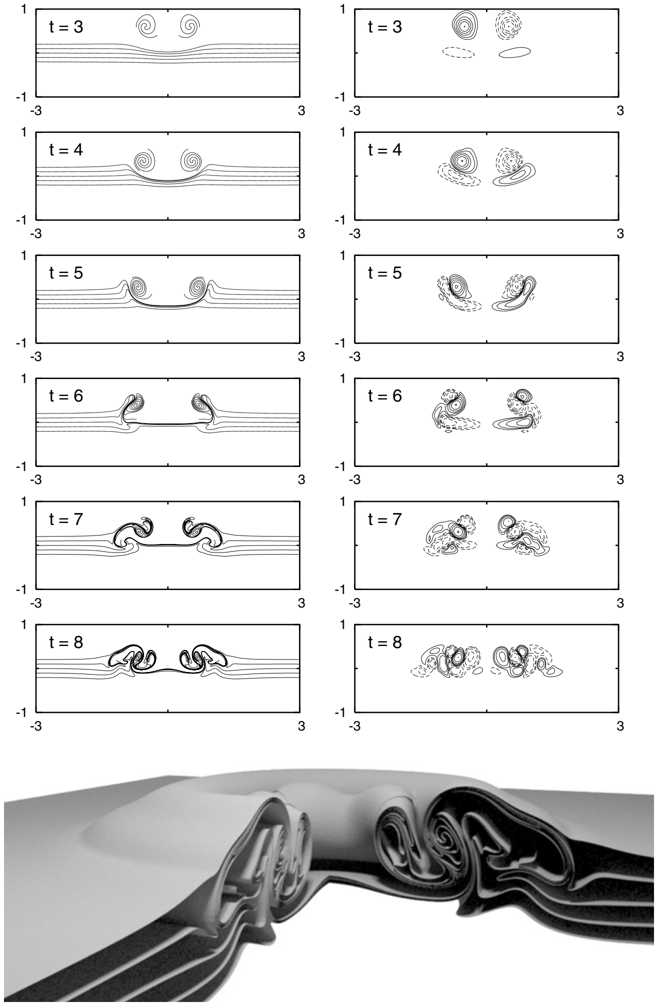

Fig. 18. Centerline slices through vortex sheet (left) and vorticity (right) for five-layer interface with $\Sigma\theta^* = 1$; $\delta^* = 0.2$, rendering is at $t^* = 8$.

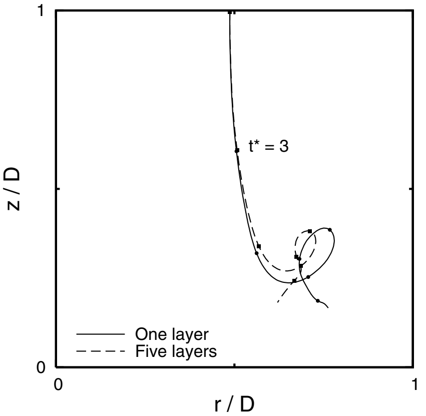

Fig. 19. Position of center of vorticity of vortex ring for both one-layer interface with $\theta^* = 1$ and five-layer interface with $\Sigma\theta^* = 1, \delta^* = 0.2$, dots every $\Delta t^* = 1$.

transfer of energy between the vortex rings of positive and negative circulation that were created over the course of the simulation. Further numerical experiments should be conducted to strengthen this hypothesis. Finally, the total circumferential circulation for both cases is nearly identical for the duration of the simulations, with a slight negative dip near the end of the thick interface simulation.

4.4. Summary

Above are presented results from inviscid simulations of vortex rings impacting normal to sharp and thick density interfaces in the Boussinesq limit. The dynamics span a range from purely passive convection and entrainment of the interface to immediate wall-like rebounding and strongly resemble the experiments in Walker et al. [49] and Dahm et al. [40]. The similarity of the dynamics of a vortex ring impinging upon a wall and a strong density interface (high θ^*) are noted in the experiments and simulations of [40].

In previous experiments and simulations of vortex-wall interactions, secondary and eventually tertiary vortex rings arise from the no-slip condition. In the inviscid simulations presented, this secondary vorticity is the result of baroclinic generation on the perturbed density interface. Regardless of it source, this secondary vorticity is pulled away from the surface to join the primary vortex ring, and in the process can create tertiary vorticity. In the limit of very high θ^*, the density interface behaves much like a wall and its deflection approaches zero. It is obviously not identical to a wall, though, as vortex lines can end on a wall as long as the total circulation on any circuit of the solid is zero. There is no wall in the above simulations, and no vorticity extends to infinity, so all vorticity created on the interface due to perturbations must be connected to itself, and any plane drawn through the interface must have constant circulation.

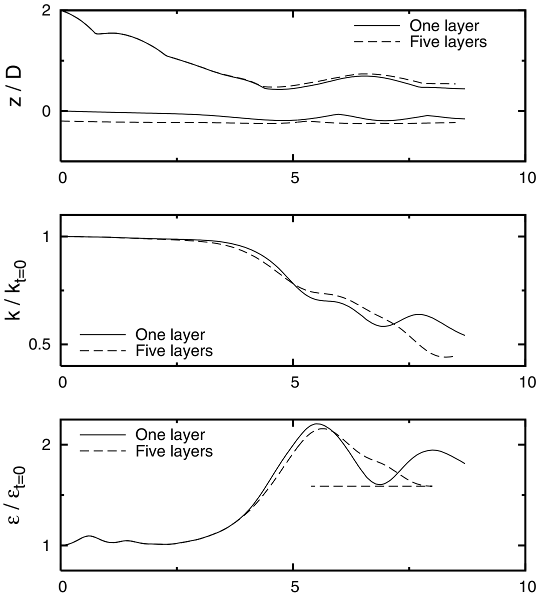

5. Conclusion

The results presented above show that an inviscid vortex sheet method can be used for simulations of the long-term, large-scale behavior of flows with weak density interfaces. This work combines elements of existing vortex methods to allow simulations to run longer than was previously possible.

The vortex sheet is discretized using a connected mesh of triangles, and element strength is defined using either vortex sheet strength or circulation depending on the stage of the calculation. This prevents errors caused by explicit calculation of the vortex stretching term, and simplifies the inclusion of alternative vorticity source terms. The remeshing method minimizes the number of elements needed to accurately describe the surface, and does not allow excessive detail below the regularization length scale. A vortex-in-cell method speeds the calculation of the velocity field and provides uniform regularization to the problem.

Avenues for future research include adapting the method to support curvature-based mesh refinement for enhanced discretization accuracy, subdivision smoothing or local corrections [68] for reducing local velocity errors, strong stratification, and surface tension. To perform simulations of flows of greater engineering interest, such as fully turbulent flows, inclusion of an explicit subfilter-scale dissipation term may also be incorporated. Some of these topics are addressed in the first author's dissertation [37] and others will be the subjects of future research.

Acknowledgment

We thank Mr. Siju Thomas for doing the Navier–Stokes simulations discussed in Section 4.2.

References

[1] G. Birkhoff, J. Fisher, Do vortex sheets roll up? Rend. Circ. Math. Palermo Ser. 2 8 (1959) 77–90.
[2] D.W. Moore, The spontaneous appearance of a singularity in the shape of an evolving vortex sheet, Proc. Roy. Soc. Lond. Ser. A 365 (1979) 105.
[3] R. Krasny, A study of singularity formation in a vortex sheet by the point-vortex approximation, J. Fluid Mech. 167 (1986) 65.
[4] A.J. Chorin, P.S. Bernard, Discretization of a vortex sheet, with an example of roll-up, J. Comput. Phys. 13 (3) (1973) 423–429.
[5] R. Krasny, Desingularization of periodic vortex sheet roll-up, J. Comput. Phys. 65 (1986) 292–313.
[6] G. Tryggvason, W.J.A. Dahm, K. Sbeih, Fine structure of vortex sheet roll-up by viscous and inviscid simulation, J. Fluids Eng. 113 (1991) 31–36.
[7] P. Luchini, R. Tognaccini, Comparisons of a viscous and inviscid numerical simulations of the start-up vortex issuing from a semi-infinite flat plate, ESAIM Proc. 7 (1999) 247–257.
[8] J.P. Christiansen, Numerical simulation of hydrodynamics by the method of point vortices, J. Comput. Phys. 13 (1973) 363–379.
[9] E. Harabetian, S. Osher, C.-W. Shu, An Eulerian approach for vortex motion using a level set regularization procedure, J. Comput. Phys. 127 (1996) 15–26.
[10] C.K. Birdsall, D. Fuss, Clouds-in-clouds, clouds-in-cells physics for many-body plasma simulations, J. Comput. Phys. 3 (1969) 494–511.
[11] B. Couët, O. Buneman, A. Leonard, Simulation of three-dimensional incompressible flows with a vortex-in-cell method, J. Comput. Phys. 39 (2) (1981) 305–328.
[12] G.-H. Cottet, M.L. Ould-Salihi, M.E. Hamraoui, Multi-purpose regridding in vortex methods, ESAIM Proc. 7 (1999) 94–103.
[13] S. Mas-Gallic, Contribution à l'analyse numérique des méthodes particulaires, Ph.D. Thesis, Université Paris VI, 1987.
[14] S. Shankar, L. van Dommelen, A new diffusion procedure for vortex methods, J. Comput. Phys. 127 (1996) 88–109.
[15] G.S. Winckelmans, A. Leonard, Improved vortex methods for three-dimensional flows, in: R.E. Caflisch (Ed.), Proceedings of the Workshop on Mathematical Aspect of Vortex Dynamics, Leesburg, Virginia, April 25–27, 1988, 1989, pp. 25–35.
[16] A. Leonard, Numerical simulation of interacting, three-dimensional vortex filaments, in: Proceedings of the IV International Conference on Numerical Methods of Fluid Dynamics, Lecture Notes in Physics, No. 35, Springer-Verlag, 1975, pp. 245–250.
[17] C. Rehbach, Numerical calculation of unsteady three-dimensional flows with vortex sheets, in: 16th AIAA Aerospace Sciences Meeting, 1978, aIAA-78-111.
[18] A.J. Chorin, Vortex models and boundary layer instability, SIAM J. Sci. Stat. Comput. 1 (1980) 1–21.
[19] R.P. Feynman, Application of quantum dynamics to liquid helium, Prog. Low Temp Phys. I (1957) 16–53.
[20] A.J. Chorin, Hairpin removal in vortex interactions, J. Comput. Phys. 91 (1990) 1–21.
[21] K. Lindsay, R. Krasny, A particle method and adaptive treecode for vortex sheet motion in three-dimensional flow, J. Comput. Phys. 172 (2001) 879–907.
[22] B. Couët, Evolution of turbulence by three-dimensional numerical particle-vortex tracing, Ph.D. Thesis, Stanford University Institute for Plasma Research, 1979.
[23] A. Leonard, Vortex methods for flow simulation, J. Comput. Phys. 37 (1980) 289–335.

[24] W.T. Ashurst, Large eddy simulation via vortex dynamics, in: Presented at the AIAA Computational Fluid Dynamics Conference, 6th, 1983, AIAA Pap. No. 83-1879-CP.

[25] A. Lozano, A. García-Olivares, C. Dopazo, The instability growth leading to a liquid sheet breakup, Phys. Fluids 10 (9) (1998) 2188–2197.

[26] D.J. Haroldsen, D.I. Meiron, Numerical calculation of three-dimensional interfacial potential flows using the point vortex method, SIAM J. Sci. Comput. 20 (1998) 648–683.

[27] C. Pozrikidis, Theoretical and computational aspects of the self-induced motion of three-dimensional vortex sheets, J. Fluid Mech. 425 (2000) 335–366.

[28] J.T. Beale, Methods for computing singular and nearly singular integrals, J. Turb. 3 (041).

[29] M. Brady, A. Leonard, D.I. Pullin, Regularized vortex sheet evolution in three dimensions, J. Comput. Phys. 146 (1998) 520–545.

[30] O.M. Knio, A.F. Ghoniem, Three-dimensional vortex simulation of rollup and entrainment in a shear layer, J. Comput. Phys. 97 (1991) 172–223.

[31] O.M. Knio, A.F. Ghoniem, The three-dimensional structure of periodic vorticity layers under non-symmetric conditions, J. Fluid Mech. 243 (1992) 353–392.

[32] O.M. Knio, A.F. Ghoniem, Vortex simulation of a three-dimensional reacting shear layer with infinite-rate kinetics, AIAA J. 30 (1) (1992) 105–116.

[33] L. Kaganovskiy, Hierarchical panel method for vortex sheet motion in three-dimensional flow, Ph.D. Thesis, University of Michigan, 2006.

[34] S.O. Unverdi, G. Tryggvason, A front-tracking method for viscous, incompressible, multi-fluid flows, J. Comput. Phys. 100 (1992) 25–37.

[35] J.-Z. Wu, A theory of three-dimensional interfacial vorticity dynamics, Phys. Fluids 7 (10) (1995) 2375–2395.

[36] C.S. Peskin, Numerical analysis of blood flow in the heart, J. Comput. Phys. 25 (1977) 220–252.

[37] M.J. Stock, A regularized inviscid vortex sheet method for three-dimensional flows with density interfaces, Ph.D. Thesis, University of Michigan, 2006.

[38] P. Swarztrauber, R. Sweet, Efficient FORTRAN subprograms for the solution of elliptic partial differential equations, Tech. Rep. NCAR Technical Note-TN/IA-109, NCAR, <http://www.scd.ucar.edu/css/software/fishpack/>, July 1975.

[39] P.F. Linden, The interaction of a vortex ring with a sharp density interface: a model for turbulent entrainment, J. Fluid Mech. 60 (1973) 467–480.

[40] W.J.A. Dahm, C.M. Scheil, G. Tryggvason, Dynamics of vortex interaction with a density interface, J. Fluid Mech. 205 (1989) 1–43.

[41] G. Tryggvason, Vortex dynamics of stratified flows, in: R.E. Caflisch (Ed.), Proceedings of the Workshop on Mathematical Aspect of Vortex Dynamics, Leesburg, Virginia, April 25–27, 1988, 1989, pp. 160–170.

[42] G. Tryggvason, S.O. Unverdi, M. Song, J. Abdollahi-Alibeik, Interaction of vortices with a free surface and density interfaces, in: C. Anderson, C. Greengard (Eds.), Vortex Dynamics and Vortex Methods, Lectures in Applied Mathematics, No. 28, American Mathematical Society, 1991, pp. 679–699.

[43] G. Tryggvason, Deformation of a free surface as a result of vortical flows, Phys. Fluids 31 (1988) 955–957.

[44] W.W. Willmarth, G. Tryggvason, A. Hirsa, D. Yu, Vortex pair generation and interaction with a free surface, Phys. Fluids A 1 (1) (1989) 170–172.

[45] G. Tryggvason, J. Abdollahi-Alibeik, W.W. Willmarth, A. Hirsa, Collision of a vortex pair with a contaminated free surface, Phys. Fluids A 4 (6) (1992) 1215–1229.

[46] D.L. Marcus, J.B. Bell, Numerical simulation of a viscous vortex ring interaction with a density interface, Phys. Fluids 6 (4) (1994) 1505–1514.

[47] C.H. Liu, A three-dimensional vortex particle-in-cell method for vortex motions in the vicinity of a wall, Intl. J. Num. Meth. Fluids 37 (5) (2001) 501–523.

[48] C.H. Liu, Vortex simulation of unsteady shear flow induced by a vortex ring, Comput. Fluids 31 (2) (2002) 183–207.

[49] J.D.A. Walker, C.R. Smith, A.W. Cerra, T.L. Doligalski, The impact of a vortex ring on a wall, J. Fluid Mech. 181 (1987) 99–140.

[50] P. Orlandi, R. Verzicco, Vortex rings impinging on walls: axisymmetric and three-dimensional simulations, J. Fluid Mech. 256 (1993) 615–646.

[51] J.D. Swearingen, J.D. Crouch, R.A. Handler, Dynamics and stability of a vortex ring impacting a solid boundary, J. Fluid Mech. 297 (1995) 1–28.

[52] T. Naitoh, O. Banno, H. Yamada, Longitudinal vortex structure in the flow field produced by a vortex ring impinging on a flat plate, Fluid Dynam. Res. 28 (1) (2001) 1–74.

[53] T. Leweke, M.C. Thompson, K. Hourigan, Vortex dynamics associated with the collision of a sphere with a wall, Phys. Fluids 16 (9) (2004) L74–L77.

[54] C. Tung, L. Ting, Motion and decay of a vortex ring, Phys. Fluids 10 (5) (1967) 901–910.

[55] P.G. Saffman, Approach of a vortex pair to a rigid free surface in viscous fluid, Stud. Appl. Math. 49 (4) (1970) 371–380.

[56] L.E. Fraenkel, Examples of steady vortex rings of small cross-section in an ideal fluid, J. Fluid Mech. 51 (1972) 119–135.

[57] J. Norbury, A family of steady vortex rings, J. Fluid Mech. 57 (1973) 417–431.

[58] M. Nitsche, Evolution of a cylindrical and a spherical vortex sheet, ESAIM Proc. 1 (1996) 401–414.

[59] R. Krasny, M. Nitsche, The onset of chaos in vortex sheet flow, J. Fluid Mech. 454 (2002) 47–69.

[60] P. Orlandi, Vortex dipole rebound from a wall, Phys. Fluids A 2 (8) (1990) 1429–1436.

[61] J.A. Luton, S.A. Ragab, The three-dimensional interaction of a vortex pair with a wall, Phys. Fluids 9 (10) (1997) 2967–2980.

[62] T.T. Lim, On the role of Kelvin–Helmholtz-like instability in the formation of turbulent vortex rings, Fluid Dynam. Res. 21 (1) (1997) 47–56.
[63] I. Eames, S.B. Dalziel, Dust resuspension by the flow around an impacting sphere, J. Fluid Mech. 403 (2000) 305–328.
[64] J. Han, G. Tryggvason, Secondary breakup of liquid drops in axisymmetric geometry Part I, constant acceleration, Phys. Fluids 11 (1999) 3650–3667.
[65] J. Han, G. Tryggvason, Secondary breakup of liquid drops in axisymmetric geometry Part II, impulsive acceleration, Phys. Fluids 13 (2001) 1554–1565.
[66] A.F. Ghoniem, G. Heidarinejad, A. Krishnan, Numerical simulation of a thermally stratified shear layer using the vortex element method, J. Comput. Phys. 79 (1988) 135–166.
[67] J. Reinaud, L. Joly, P. Chassaing, Numerical simulation of a variable-density mixing-layer, ESAIM Proc. 7 (1999) 359–368.
[68] C.R. Anderson, A method of local corrections for computing the velocity field due to a distribution of vortex blobs, J. Comput. Phys. 62 (1986) 111–123.